Stability of van der Waals $FePX_3$ materials (X: S, Se) for water-splitting applications

Sandhya Sharma[1], Hafiz Muhammad Zeeshan[1], Mohammad Panahi[1], Yichen Jin[2,3], Mouhui Yan[2,3], Yukun Jin[2,3], Kexin Li[2,3], Patrick Zeller[4,5], Anna Efimenko[6,7], Anna Makarova[8], Dmitry Smirnov[9], Elena Voloshina[2,1,8,*] and Yuriy Dedkov[3,2,1,*]

[1]Centre of Excellence ENSEMBLE3 Sp. z o.o., Wolczynska Str. 133, 01-919 Warsaw, Poland

[2]Department of Physics, Shanghai University, 99 Shangda Road, 200444 Shanghai, China

[3]Materials Genome Institute, Shanghai University, 99 Shangda Road, 200444 Shanghai, China

[4]Helmholtz-Zentrum Berlin für Materialien und Energie, Elektronenspeicherring BESSY II, Albert-Einstein-Str. 15, 12489 Berlin, Germany

[5]Department of Inorganic Chemistry, Fritz-Haber-Institut der Max-Planck-Gesellschaft, Faradayweg 4-6, 14195 Berlin, Germany

[6]Interface Design, Helmholtz-Zentrum Berlin für Materialien und Energie GmbH (HZB), Albert-Einstein-Str. 15, 12489 Berlin, Germany

[7]Energy Materials In-situ Laboratory Berlin (EMIL), Helmholtz-Zentrum Berlin für Materialien und Energie GmbH (HZB), Albert-Einstein-Str. 15, 12489 Berlin, Germany

[8]Institut für Chemie und Biochemie, Freie Universität Berlin, Arnimallee 22, 14195 Berlin, Germany

[9]Institut für Festkörper- und Materialphysik, Technische Universität Dresden, 01069 Dresden, Germany

E-mail: `elena.voloshina@icloud.com; yuriy.dedkov@icloud.com`

Abstract.

The interaction of high-quality transition metal trichalcogenides (TMTs) single crystals $FePX_3$ (X: S, Se) with water molecules is studied using near-edge X-ray absorption fine structure (NEXAFS) and X-ray photoelectron spectroscopy (XPS) in a wide range of temperature and partial pressure of H_2O. The physisorption nature of interaction between H_2O and $FePX_3$ is found at low temperatures and relatively small concentrations of water molecules, that is supported by the DFT results. When temperature of the $FePX_3$ samples and partial pressure of H_2O are increased, the interaction at the interface is defined by two competing processes – adsorption of molecules at high partial pressure of H_2O and desorption of molecules due to the increased surface mobility and physisorption nature of interaction. Our intensive XPS/NEXAFS experiments accompanied by DFT calculations bring new understanding on the interaction of H_2O with surface of a new class of 2D materials, TMTs, pointing to their stability and reactivity, that is important for further applications in different areas, like sensing and catalysis.

1. Introduction

Electrocatalytic water splitting with production of hydrogen (H_2), which is presently considered as an alternative to traditional fossil fuels in industry and transportation, involves two half-reactions, the hydrogen evolution reaction (HER) at the cathode and oxygen evolution reaction (OER) at the anode [1, 2, 3]. The unfavourable thermodynamics and sluggish kinetics of these reactions impede efficient H_2 production. So far scarce precious metals (Pt, Ru and Ir oxides) are used as electrodes [4, 5]. Their replacement is obviously a major concern, and the matter of considerable efforts. The possible candidates include materials based on transition metals (oxides, chalcogenides, nitrides, phosphides, carbides) and non-metal catalysts (e. g. graphene, g-C_3N_4) [6, 7, 8, 9, 10, 11].

A drastic cut in the energy cost for H_2 production can be realized upon switching from electrocatalytic to photocatalytic water splitting. In this way the two reactions occurring at the photocatalyst are: (1) $2H^+ + 2e^- \rightarrow H_2$ and (2) $2H_2O + 4h^+ \rightarrow 4H^+ + O_2$, where e^- and h^+ are a photo-generated electron and hole, respectively [3, 12, 13]. Suitable photocatalytic materials are semiconductors, with the best possible interaction with light via electron-hole pairs (excitons), a bandgap spanning the UV-vis range ($1.59 - 6.20\,\mathrm{eV}$), and bandgap edges below and above the H^+/H_2 and O_2/H_2O redox potentials [14]. Relevant materials are designed in the form of high specific area structures, providing easy access to the large number of catalytic active sites. This includes nano/meso-porous materials of two-dimensional (2D) zeolites and metal-organic frameworks (MOF) [15], as well as lamellar compounds like graphene-like carbon nitride [16], semiconducting di- and tri-chalcogenides of transition metals [17, 18], and layered double hydroxides [19]. In these lamellar compounds, the reactant (water) and products (hydrogen, oxygen) readily intercalate and de-intercalate through the 2D nanogap between the individual layers of the materials, while each layer has essentially all its atoms and catalytic active sites exposed.

Very recently, the MPX_3 materials (transition metal trichalcogenides, TMTs; M: transition metal, X: chalcogen) appeared as promising candidates for clean energy generation and related photocatalytic water splitting applications, because of their suitable band gaps and charge carrier mobility [20, 21]. The theoretically predicted band gaps were confirmed experimentally [22, 23, 24]. Strikingly, MPX_3 materials provide a wide spectrum of opportunities to adjust the efficiency of the water splitting reaction using band structure engineering, tuning of the charge carrier density, fast charge transfer kinetic, and low energy for chemisorption of various intermediate species on the MPX_3-based catalyst surfaces [18, 20, 25, 26]. Each individual layer of the MPX_3 compound exhibits phosphorous and chalcogen atoms at their two faces, in the form of PX_3 three-leg stars (Fig. 1(a,b)). The immediate proximity of the two kinds of atoms has synergetic effects on the electronic properties of the metallic honeycomb lattice sitting in the median plane of each layer. By using different transition metals (Mn, Fe, Ni, etc.) and chalcogens (S, Se), a wide range of electronic and magnetic properties

can be covered [22, 27, 28, 23, 24, 29, 30, 31, 32]. Properties may be further engineered by intercalating foreign species (alkali atoms, functional molecules) within the van der Waals gap between the individual layers [33, 34, 35].

Some of MPX_3 materials were tested for the photo-hydrogen evolution in pure water. For example, few-layered $NiPS_3$ and $FePS_3$ demonstrated a constant evolution rate of $\approx 26\,\mu\mathrm{mol\,g^{-1}h^{-1}}$ and $\approx 290\,\mu\mathrm{mol\,g^{-1}h^{-1}}$, respectively, which however is still about an order of magnitude lower than that of the MoS_2-based materials and Ni/Cu-modified titania [36, 37]. Also, these measurements of the hydrogen evolution over 40 h indicated that $FePS_3$ quantum sheets are more stable than the $NiPS_3$ ones. Surprisingly, the existing theoretical and experimental works, focused on the photocatalytic properties of MPX_3 compounds, which reveal several promising predictions and observations also demonstrate the unexplored areas of investigation and very often do not contain any insight in the electronic structure and surface interaction with different species. Also there is a lack of systematic spectroscopic studies on the studies of the interaction of MPX_3 with water molecules or other gaseous species. Obviously, for the basic understanding, the investigations from fundamental experiments in vacuum to close-to-atmospheric conditions ("bridging the pressure gap") are indispensable to establish the relevance of MPX_3 materials for water splitting applications.

Here, we present the first systematic spectroscopic studies of the water interaction with surfaces of high quality bulk $FePX_3$ materials (X: S, Se). In the presented experiments the interaction with water molecules was studied in the water partial pressure range between ultra-high vacuum (UHV) conditions and 1 mbar and sample temperature up to 300° C. It is found that at low temperatures, the adsorption of H_2O on $FePX_3$ has a physisorption nature that is also confirmed by the accompanied density functional theory (DFT) calculations. The interaction of $FePX_3$ with H_2O in the high-pressure region is temperature dependent and is determined by two competing processes – adsorption of H_2O at high partial pressure and desorption of molecules due to the increased surface mobility and physisorption nature of interaction. It is found that, contrary to $FePSe_3$, the $FePS_3$ TMT material is quite stable in the very wide range of water partial pressure and temperature indicating its high perspective in photoelectrochemical water-splitting applications. Our experimental results are accompanied by the intensive large-scale DFT calculations supporting main experimental findings.

2. Experimental and computational details

The detailed description of synthesis and characterization of bulk $FePX_3$ (X: S, Se) is presented in Ref. [29]. Briefly, we employed the chemical vapour deposition method using the stoichiometric amounts of chemicals. Subsequently, all samples were routinely characterized in the laboratory conditions using different methods: optical microscopy, x-ray diffraction (XRD), transmission electron microscopy (TEM), scanning electron microscopy combined with energy dispersive x-ray analysis (SEM/EDX), and Raman

spectroscopy [29].

Laboratory-based X-ray photoelectron spectroscopy (XPS) experiments were performed in the UHV station installed in Shanghai University and consisting of preparation and analysis chambers with a base pressure better than 1×10^{-10} mbar (SPECS Surface Nano Analysis GmbH). XPS spectra were collected using monochromatized Al K_α ($h\nu = 1486.6$ eV) X-ray source and SPECS PHOIBOS 150 hemispherical analyser combined with a 2D-CMOS detector. All $FePX_3$ samples were glued on the Mo sample holder using conductive silver paste and then, prior every set of measurements of XPS spectra, samples were cleaved in the UHV conditions directly in the analysis chamber. This procedure allows to prepare clean and ordered surfaces of $FePX_3$ crystals free of C- and O-contamination. All XPS spectra obtained in the laboratory are in very good agreement with previously published results and were used as references for further experiments.

Temperature stability experiments on $FePX_3$ were performed at the FlexPES beamline at the MAXIV synchrotron radiation facility (Lund). All spectra were measured in the UHV conditions (base vacuum is below than 5×10^{-10} mbar). Before every set of experiments, new sample was cleaved in air and quickly introduced in vacuum, followed by the degassing routine at 350° C for 60 min. XPS core-level and valence band spectra were acquired using ScientaOmicron DA30 analyser combined with a 2D-CCD detector. Photon energies in all experiments were calibrated using a polycrystalline Au sample. Temperature of the sample during experiments was monitored using calibrated K-type thermocouple.

Photoelectron spectroscopy measurements at the BESSY II electron storage ring operated by the Helmholtz-Zentrum Berlin für Materialien und Energie were performed at two different beamlines equipped with the respective experimental stations: (i) Investigations of the water adsorption on $FePX_3$ at low temperatures were carried out at the Russian-German dipole soft X-ray beamline (RGBL-dipole) [38] and (ii) near-ambient pressure (NAP) photoelectron spectroscopy experiments on the water interaction with $FePX_3$ were performed at the CAT branch of the dual-color Energy Materials In-Situ Laboratory Berlin (EMIL) beamlines [39, 40]. At RGBL-dipole all spectra were measured in the UHV conditions (vacuum level is below than 2×10^{-10} mbar). Before every set of experiments, new sample was introduced in vacuum, followed by the degassing routine at 350° C for 60 min. Near-edge X-ray absorption fine structure (NEXAFS) spectra were collected in the partial electron yield (PEY) mode using channel plate detector (repulsive potential $U = -80... - 100$ V). XPS core-level and valence band spectra were acquired using SPECS PHOIBOS 150 analyser combined with a 2D-CCD detector. Photon energies in all experiments were calibrated using a polycrystalline Au sample. At CAT beamline NAP-XPS/NEXAFS experiments were carried out with two undulators, UE48 and CPMU17, for soft and hard X-rays, respectively, and the experimental station equipped with a SPECS PHOIBOS 150 NAP analyzer and a 2D-CMOS detector. The base pressure in the experimental station is in the range of 5×10^{-8} mbar. In this case $FePX_3$ samples were mounted on the

sample holder without any additional *ex situ* or *in situ* surface treatment. Samples were heated from the back side of the sample holder using infrared laser and temperature was controlled via feedback-loop using K-type thermocouple. In the NAP-XPS experiments core-level XPS spectra were collected with kinetic energies in the range of $150 - 250\,\mathrm{eV}$ and NEXAFS spectra were acquired using hemispherical energy analyser in the Auger-electron yield (AEY) mode giving in both cases the high surface sensitivity of the obtained results. The specific parameters, like sample temperature, water dose and working pressures are explicitly discussed in the corresponding places of manuscript.

The spin-polarized DFT calculations were carried out with the Vienna *ab initio* simulation package (VASP) [41, 42, 43], employing the generalised gradient approximation (GGA) functional of Perdew, Burke and Ernzerhof (PBE) [44]. The ion-cores were described by projector-augmented-wave (PAW) potentials [45] and the valence electrons [Fe ($3p$, $3d$, $4s$), P ($3s$, $3p$), S ($3s$, $3p$), and Se ($4s$, $4p$)] were described by plane waves associated to kinetic energies of up to $500\,\mathrm{eV}$. Brillouin-zone integration was performed on Γ-centred symmetry with Monkhorst-Pack meshes by Gaussian smearing with $\sigma = 0.05\,\mathrm{eV}$ except for density of states (DOS) calculations, where the tetrahedron method with Blöchl corrections was employed [46]. The $12\times12\times4$ and $12 \times 12 \times 1$ k-meshes were used for the studies of bulk and monolayer $FePX_3$, respectively. The structures were fully relaxed until forces became smaller than $0.01\,\mathrm{eV\,Å^{-1}}$. The convergence criteria for energy was set equal to $10^{-5}\,\mathrm{eV}$. For the structure optimisation, the DFT+U scheme [47, 48] was adopted for the treatment of Fe $3d$ orbitals, with the parameter $U_{\mathrm{eff}} = U - J$ equal to $3\,\mathrm{eV}$. The adsorption energies as well as density of states were computed using the Heyd, Scuseria, and Ernzerhof (HSE) hybrid functional [49]. This functional uses 25 % Fock and 75 % PBE exchange energy and a screening parameter of $0.207\,\mathrm{Å^{-1}}$. The van der Waals interactions were incorporated by the semi-empirical approach of Grimme through the D2 correction [50]. Functional specific global scaling factors for the dispersion contribution of 0.75 and 0.60 were employed in PBE+U and HSE calculations, respectively.

When modelling $FePX_3$ monolayers, the lattice constant in the lateral plane was set according to the optimised lattice constant of bulk $FePX_3$ [29]. A vacuum gap was set to approximately 26 Å. The electrically neutral vacancies were created by removing one X atom from the (2×2) supercells. Thereby, the distance between repeated vacancies in the nearest-neighbour cells is larger than 10 Å. The defect formation energy is defined as follows: $\Delta E_{\mathrm{def}} = E(\mathrm{FePX_{3\text{-}n}}) + \mu_X - E(\mathrm{FePX_3})$, where $E(\mathrm{FePX_{3\text{-}n}})$ and $E(\mathrm{FePX_3})$ are the energies of the 2D $FePX_3$ with and without vacancy, respectively, μ_{X} is the chemical potential of X atom. To study the adsorption of a single molecule, a (2×2) supercell was used with one water molecule added. Adsorption energies were calculated as $\Delta E_{\mathrm{ads}} = E(A/B) - [E(A) + E(B)]$, where $E(A)$ and $E(B)$ are the energies of the isolated 2D $FePX_3$ and an adsorbate, and $E(A/B)$ is the energy of their interacting assembly.

3. Results and Discussion

DFT. In layered bulk $FePX_3$ crystals the monolayers stack in the $C2/m$ and $R\overline{3}$ space groups with the van der Waals gap of 3.32 Å and 3.26 Å between neighboring chalcogen layers for X = S and X = Se, respectively [29]. Both 3D $FePX_3$ compounds adopt the antiferromagnetic (AFM) ground states. The coincidence of ionic and covalent interactions in the structural unit of $FePX_3$ leads to the unique distribution of valence band states in the calculated DOS distributions. Both $FePX_3$ compounds are wide band gap semiconductors with an energy gap of 2.09 eV and 1.64 eV for X = S and X = Se, respectively (Fig. 1(c) and Fig. S1(a)). The top of the valence band of $FePX_3$ is formed by the hybrid Fe-S/Se states with almost equal contribution of the Fe-3d and S/Se-p partial DOS. The bottom of the conduction band is formed by Fe-d states with admixture of the chalcogen p states. At the same time the less localized character of the electronic states, and particularly of the Fe-d states, can be noted in case of X = Se. The character of states stays unchanged when switching from bulk to monolayers (cf. Fig. 1(c) and (d)), only the band gaps are slightly larger than the values calculated for the bulk phases and are 2.45 eV and 2.07 eV for 2D $FePS_3$ and 2D $FePSe_3$, respectively, due to the quantum confinement effects. (For the DOS of 2D $FePSe_3$, see Fig. S1(b)). The ground state configuration for the 2D $FePX_3$ monolayers is AFM with zig-zag ordering of spin states.

Mechanical exfoliation, which is used for the monolayer production or surface cleaning, can lead to formation of chalcogen vacancies. Usually, several types of vacancies are considered. According to our previous studies, the so-called V_X@1L defects (one vacancy at X-site) are the most favourable to form [28, 51, 52] and in the present study we restricted ourselves to this kind of defects. The defect formation energy in this case is found to be 1.23 eV and 1.02 eV for X = S and Se, respectively, and this is in trend with the previously calculated values for the other MPX_3 monolayers [28, 51, 52]. Removal of chalcogen atom leads to some modifications of the local lattice and electronic structures. As compared to the pristine $FePX_3$ monolayer, the phosphorous dimers tend to move closer to the vacancy. The angle, which P–P dimer forms with the vertical direction is 3.6° and 4.8° for X = S and Se, respectively. Moreover, the dimer is pulled out from a monolayer, yielding somewhat increase of the P–S bond length (by ≈ 0.05 Å), whereas the P–P bond lengths stays almost unchanged.

The electrons left behind upon removal of a chalcogen atom, occupy the easily available electronic states of a (P_2X_5) entity. In the case of $FePS_3$, a well-localized defect state generated within the energy gap just below the Fermi energy (Fig. 1(e)). In the case of $FePSe_3$, this state is not well-localized, but its signature can be visible in the vicinity of E_F (Fig. S1(c)). For both monolayers under study, one more state is formed in the energy gap above E_F and it has Fe-3d character. As a result, the energy gap width of the defective monolayers somewhat decreased to $E_g = 2.04$ eV and 1.81 eV for $FePS_{3\text{-}x}$ and $FePSe_{3\text{-}x}$, respectively.

The effect of adsorption of molecular water plays an important role in various

applications and can affect the electronic properties of $FePX_3$ monolayers. Thus, in the next step we investigate the adsorption of a single H_2O molecule on pristine and defective $FePX_3$ monolayers considering different high-symmetry adsorption sites and adsorption orientations. For the pristine monolayers, all adsorption configurations have similar adsorption energies which range from -133 meV to -209 meV and from -112 meV to -207 meV for 2D $FePS_3$ and 2D $FePSe_3$, respectively. In the relaxed structures water stays almost parallel to the substrate and the vertical distance between the molecule and the $FePX_3$ monolayer is always above 3.2 Å. The most stable adsorption structure denoted as **AS1** is presented in Fig. 2(a). Here, a water molecule stays above a P atom ($d_{\mathrm{P-O}} = 3.21$ Å and 3.30 Å for $FePS_3$ and $FePSe_3$, respectively) and the H atoms are directed towards the neighbouring X atoms. In accordance with the weak interaction, the structural parameters of H_2O as well as of the studied monolayers undergo insignificant changes. As follows from the electron density redistribution plot (Fig. 2(a)), the main charge rearrangement upon adsorption takes place between O and P atoms. Charge accumulation in the p-orbital of P on the side of the adsorbate indicates that it is the main orbital participating in the bonding. Simultaneously, one notes the charge depletion at the hydrogen positions. These observations are in line with the effects arising in DOS due to the interaction between H_2O and $FePX_3$ (Fig. 2(b)): hybridization between p states of P and the water lone pair (the $1b_1$ molecular orbital of H_2O) takes place, resulting in broadening of the respective water derived state. (For the DOS of $H_2O/FePSe_3$, see Fig. S1(d)). The obtained results on the adsorption of H_2O on pristine $FePX_3$ are in general trend known for the other MPX_3 materials [51, 52].

The adsorption structure similar to **AS1** can be realised also in the case of defective $FePX_3$ monolayers. It is abbreviated as **AS2** and presented in Figure 2(c). In this case, the interaction between the water molecule and the substrate is stronger ($\Delta E_{\mathrm{ads}} = -272$ meV and $\Delta E_{\mathrm{ads}} = -277$ meV, for X = S and Se respectively), which is reflected by the reduced distance $d_{\mathrm{P-O}} = 3.00$ Å and 3.11 Å for $FePS_3$ and $FePSe_3$, respectively. In the rest, the electronic structures of the molecule and substrate undergo qualitatively similar changes as in the case of **AS1** (Fig. 2(d) and Fig. S1(e)).

In addition, a structure **AS3** was investigated, where water molecule is coordinated between two Fe ions as it is shown in Figure 2(e). This adsorption structure is characterised by $\Delta E_{\mathrm{ads}} = -712$ meV and $\Delta E_{\mathrm{ads}} = -755$ meV, for X = S and Se respectively. The stronger adsorption as compared to **AS2** is related (i) to the higher coordination of the molecule in the vacancy and (ii) quite strong interaction between the water H atom and the P atom, which lost the chalcogen neighbour. As a proof, one notes a strong accumulation of electron density between O and two Fe ions as well as between H and P atoms (Fig. 2(e)). Analysis of the partial DOS (Fig. 2(f) and Fig. S1(f)) shows that, the orbitals of water contribute significantly to the $FePX_3$ defect states.

A closer look at **AS3** reveals some changes in the molecular structure: a significant elongation of the H–O bond from 0.97 Å for the gas-phase molecule to 1.06/0.98 Å and 1.04/0.98 Å for the adsorbed molecule on $FePS_{3\text{-}x}$ and $FePSe_{3\text{-}x}$, respectively. As a

result of the interaction with the monolayer, the angle H–O–H is enhanced to 111.5° and 110.4° in the case of $H_2O/FePS_{3\text{-}x}$ and $H_2O/FePSe_{3\text{-}x}$ with respect to the gas phase H_2O molecule (104.5°). A further O–H bond elongation up to d(O–H) = 1.70 Å leads to structure **AS4** (Fig. 2(g)), which is slightly higher in energy as compared to **AS3** ($\Delta E_{\text{ads}} = -649$ meV). Here the P–H bond is formed (d(P–H) = 1.42 Å). The hydroxyl group in the vacancy shows an accumulation in the 1π orbital and depletion in the 3σ orbital (Fig. 2(g)). Charge accumulation between P and H is also detected. The observed phenomena can also be seen in partial DOS (Fig. 2(h)). The corresponding structure was found to be unstable for $FePSe_{3\text{-}x}$.

UHV-XPS/NEXAFS. Figure 3 presents the summary of bulk $FePX_3$ crystals characterization in the laboratory conditions. All layered crystals used in the present study have typical dimensions of about 5mm × 5mm and are of hexagonal symmetry, which can be clearly depicted from the optical images, where step edges form angles of 60° or 120° [29, 53] (see Fig. 3(a-d)). XRD data confirm that bulk $FePX_3$ crystallize within the $C2/m$ and $R\overline{3}$ space symmetry groups for X = S and X = Se, respectively (Fig. 3(e)). After the UHV cleavage of bulk $FePX_3$ the resulting surfaces show no C- and O-contaminations (Fig. 3(f)). The positions of main XPS lines measured with respect to the valence band maximum (VBM) for every $FePX_3$ compound (Fig. 3(g-j)) are summarized in Table 1. The respective differences for the binding energies of the Fe $2p$ and P $2p$ XPS lines can be assigned to the slight difference of electronegativity for S and Se. The Fe $2p$ spectrum demonstrates a series of satellites which can be assigned to different final states and these spectra are in very good agreement with previously published and discussed data [29, 54] as well as similar to those for FeO [55, 56] indicating the Mott-Hubbard insulating state of $FePX_3$. The valence band spectra of $FePX_3$ (Fig. 3(g)) show a main emission band in the energy range $E - E_{VBM} < -5$ eV and a series of satellites at higher binding energies, which is typical for this class of compounds [24, 29, 30]. The recent resonant photoemission experiments accompanied by the DFT calculations confirm the Mott-Hubbard insulating state of $FePX_3$ and indicate that the top of the valence band is formed by Fe $3d$ – S $3p$/Se $4p$ hybrid electronic states [29]. This behaviour of $FePX_3$ is opposed, for example, to the case of the isostructural layered $NiPS_3$ TMT which is identified as a charge-transfer insulator [24] and can be taken as an indicator that the former TMT might be considered as a perspective materials for the photoelectrochemical water splitting applications [18, 57, 58].

Experiments on the temperature stability of $FePX_3$ were performed at FlexPES beamline of MAX IV, where photoemission spectra were measured in the fixed mode of the energy analzer as a function of $FePX_3$ samples temperature. The results of these experiments are compiled in Fig. 4 where single photoemission spectra before and after annealing of $FePS_3$ at 550° C are shown in (a-e) and the respective temperature dependent photoemission intensity maps are presented in panels (f-i) (the intensity drop at high temperatures in the XPS intensity maps is caused by the rapid increase of the pressure in the analysis chamber due to the sample's materials evaporation). From the

temperature-dependent intensity maps one can clearly see that samples remain stable up to $(502 \pm 2)^\circ$ C when the intensive evaporation of S starts as can be monitored by the energy shift of the respective photoemission lines as well as by the decrease of the photoemission signal of S $2p$ and P $2p$. Further increase of the samples' temperature to 520° C leads to the samples' decomposition and significant losses of S and P. At the same time the loss of the samples' stoichiometry leads to the restore of the metallic edge in the valence band and the Fe $2p$ XPS spectrum is very similar to the one for the non-stoichiometric iron phosphide, Fe_xP_y [59, 60].

The interaction of water molecules with $FePX_3$ and stability of surfaces were initially studied in the experimental station at the RGBL-dipole beamline in UHV conditions. Here, surfaces of $FePX_3$, prepared as described in the previous section, were exposed to 10 L (L = Langmuir) of H_2O at 120 K. Such dose, as expected, guarantees the complete coverage of the samples' surfaces with, at least, one molecular layer of H_2O. The respective XPS and NEXAFS spectra of $FePX_3$ collected before after H_2O exposure are shown in Figs. 5 and 6.

Before deposition of H_2O, XPS spectra of $FePX_3$ show the presence of oxygen- and carbon-related emission lines, which are assigned to the residual contamination arising from the respective samples' preparation routine used in these experiments (Fig. 5(a)). The small P_xO_y-related peak at $E - E_{VBM} \approx -133.6$ eV, which can be attributed to the respective surface contaminations is also visible in the corresponding P $2p$ spectra of $FePX_3$, see panel (c). After adsorption of H_2O molecules on the surface of $FePX_3$ the intensity of the main XPS emission lines for the $FePX_3$ materials is reduced. However, the low temperature adsorption of water molecules does not change the shape and positions of these XPS lines. This can be clearly deduced from the analysis of all high-resolution core level XPS spectra shown in Fig. 5(b-d). Also, the respective XPS spectra of the valence band region, main emission bands at $E - E_{VBM} < -5$ eV and the satellites structure, are not strongly affected. However, after adsorption of water molecules a new broad peak appears in the P $2p$ XPS spectra centred at $E - E_{VBM} = -133.75 \pm 0.02$ eV, which can be attributed to the P-O bonds. Taking into account that Fe $2p$ and S $2p$/Se $3p$ XPS spectra of $FePX_3$ are not strongly affected by the adsorption of water molecules, we can conclude that H_2O is physisorbed above $FePX_3$ at the positions of the P-P dimers with the O-atoms pointing to the P-atoms. These conclusions are in good agreement with the DFT results presented above. The physisorption of water molecules on the surface of layered $FePX_3$ materials is also confirmed by the recovery of all XPS spectra (not shown) after desorption of H_2O when sample is warmed to the room temperature.

The similar conclusion can be made after analysis of the NEXAFS spectra acquired in the PEY mode for the $FePX_3$ samples before and after water adsorption as shown in Fig. 6 and Fig. S2 of Supplementary Materials for the Fe $L_{2,3}$ and P $L_{2,3}$ absorption edges, respectively. The NEXAFS spectra of $FePX_3$ were discussed in details in Ref. [29] and they confirm the Mott-Hubbard state of TMT materials. After adsorption of H_2O on $FePX_3$ the NEXAFS spectra collected at both absorption edges in the PEY mode demonstrate no significant changes indicating the physisorption nature of interaction at

the $H_2O/FePX_3$ interface at low temperatures.

NAP-XPS/NEXAFS. Further studies on the interaction of water with surface of the $FePX_3$ materials were performed in the NAP-XPS/NEXAFS experiments at the CAT@EMIL beamline of BESSY II. The temperature/H_2O-partial-pressure sequence during measurements is schematically shown in Fig. 7. The results of these experiments are summarized in Figs. 8 and 9 for $FePS_3$ (in Figs. S3 and S4 of Supplementary Materials for $FePSe_3$).

Initial NAP-XPS spectra of $FePX_3$ measured at room temperature and in the absence of water demonstrate the presence of photoemission lines which can be assigned to the adsorbed residual oxygen-derived contaminations due to the respective samples' treatment before experiments (see previous discussions). In the presence of 0.1 mbar and 1.0 mbar of H_2O at room temperature the XPS spectra show the strong reduction of intensity of all TMT-related emission lines due to the large attenuation of the surface sensitive photoemission signals. The increased partial pressure of water leads to the significant increase of the oxygen-induced features in the respective P $2p$ and S $2p$ XPS spectra of $FePX_3$. At the same time, despite the reduced photoemission intensity and increased background of scattered electrons, the Fe $2p$ XPS spectra of $FePX_3$ do not demonstrate the appearance of new satellite peaks which can be assigned to the higher oxidations states of iron atoms. These observations can be explained by the self-protective properties of TMT layers when the inner layers of hexagonally arranged Fe atoms are sandwiched between the $[PX_3]$ layers, and thus not affected by the water adsorption.

When the temperature of $FePX_3$ is increased to 200° C, the two processes start to compete: (i) desorption of residual gas molecules and water molecules from the surface of $FePX_3$ due to the increased atoms' and molecules' mobility and (ii) adsorption of H_2O on $FePX_3$ at high partial pressure and oxidation of P and X atoms. As one can see from the XPS spectra of $FePS_3$ (Fig. 9), the first process prevails at 200° C and 0.1 mbar of H_2O, because at these parameters the S $2p$ and Fe $2p$ spectra are very similar to the ones for the clean $FePS_3$ (see Figs. 3 and 5); also the P $2p_{3/2}$ XPS signal at $E - E_{VBM} \approx -131.3$ eV which can be assigned to clean surface of $FePS_3$ is significantly increased. Still, the existence of the broad peak at $E - E_{VBM} \approx -133.5$ eV in the P $2p$ spectrum which is assigned to the oxidation of P atoms, can be explained by the adsorption of H_2O molecules preferably above P-P dimers of $FePS_3$. Further increase of the partial pressure of H_2O to 1.0 mbar leads to the increase of XPS components which are connected with a chemical interaction of S- and P-atoms with oxygen of adsorbed water molecules and the respective charge transfer. Similar treatment of the $FePSe_3$ TMT material leads to the strong oxidation of P-atoms as can be deduced from the strong intensity of the broad P_xO_y-related peak at $E - E_{VBM} \approx -133.7$ eV and to very significant reduction of the Se $3p$ signal which can be connected with the reduction of concentration of Se atoms at the $H_2O/FePSe_3$ interface (Fig. S3 of Supplementary Materials). It can be explained either by evaporation or interdiffusion of Se due to the weaker P-Se bonds compared to P-S and possible instability of $FePSe_3$ at these

experimental conditions.

Further increase of water pressure and temperature of the $FePX_3$ samples to 300° C leads to the samples' modifications as found from the XPS results. First, although as was discussed before the $FePX_3$ TMTs can be considered as self-protective materials, the Fe $2p$ XPS spectra are changed to the ones characteristic for the higher oxidation state of Fe atoms as indicated by the spectral weight redistribution for the main Fe $2p_{3/2,1/2}$ XPS lines (cf. Fe $2p$ XPS spectra @0.1 mar/200° C and @1.0 mar/200° C, @0.1 mar/300° C, @1.0 mar/300° C) [55, 56, 61]. Secondly, for both materials the increase of the temperature leads to the strong oxidation of P-atoms at 0.1 mbar and 1.0 mbar of the partial pressure of H_2O as deduced from the strong P_xO_y-related peak and from the almost disappearance of the P $2p$ attributed to the clean $FePX_3$ surface. At the same time, the interaction of H_2O with surface of $FePX_3$ via formation of the P-O bond and orientation of the H_2O molecules as shown in Fig. 2 lead to the electron accumulation on the S atoms (signature for the interaction between water hydrogens and the neighbouring chalcogen atoms) that explains the appearance of the strong shoulder at the low binding energy of the S $2p$ spectra at $E - E_{VBM} \approx -160.7$ eV.

The same conclusions can be also made from the analysis of the NAP-NEXAFS spectra of the studied systems (Fig. 9 and Fig. S4 of Supplementary Materials). The Fe $L_{2,3}$ and P K NEXFS spectra of $FePX_3$ collected at room temperature and 0.1 mbar and 1.0 mbar of partial pressure of H_2O demonstrate the increase of the intensities of the FeO_x- ($\approx$ 710.8 eV) and P_xO_y-related ($\approx$ 2155.2 eV) components in the respective absorption spectra. The increase of the samples' temperature to 200° C leads to the strong decreasing (or complete absence) of the oxygen-related features in the Fe $L_{2,3}$ and P K NEXAFS spectra and the respective spectra are similar to the ones for the clean $FePX_3$ materials (see Fig. 6 and Ref. [29]), confirming previous conclusions made from the analysis of the NAP-XPS data. After further increase of the samples temperature to 300° C, the Fe $L_{2,3}$ and P K NEXAFS spectra indicate the appearance of the oxygen-induced features in the spectra confirming the formation of a thin "dead"-layer of P_xO_y (this effect is more pronounces for $FePSe_3$, see Fig. S4 of Supplementary Materials). At the same time, the S K NEXAFS spectrum collected at 300° C and 1.0 mbar of H_2O shows the new spectral feature on the high photon energy side of the main line of the spectrum (at $\approx$ 2472.2 eV) which can be also assigned to the interaction between hydrogen atoms of H_2O and S-atoms.

4. Conclusions

In summary, the stability of high-quality $FePX_3$ crystals and their interaction with water molecules is studied using XPS and NEXAFS methods in a wide range of temperatures and partial pressures of H_2O. It is found that $FePX_3$ are stable in the UHV conditions up to $\approx$ 500° C when the significant loss of S/Se and P is observed. Our further UHV-based XPS/NEXAFS studies on the water adsorption demonstrate the physisorption nature of interaction between H_2O and $FePX_3$ at low temperature and low partial

pressure of H_2O, that is supported by the DFT results. In this case, the almost complete recovery of the surface of the $FePX_3$ crystals is observed after desorption of water when temperature is restored to room temperature. In the NAP-XPS/NEXAFS experiments when temperature of $FePX_3$ is increased to 200° C the two competing processes – adsorption at high partial pressure of H_2O and desorption of molecules due to the increased surface mobility and physisorption nature of interaction – define the observed changes in the NAP-XPS and NEXAFS spectra. Further increase of the temperature of $FePX_3$ to 300° C leads to the partial oxidation of the top layer of $FePX_3$ with a formation of the P_xO_y "dead"-layer. Our intensive UHV- and NAP-XPS/NEXAFS experiments accompanied by DFT results are the first spectroscopic studies of the water interaction with surface of this new class of 2D materials addressing their stability, the aspect which is important for further applications of TMT materials in different areas, like electronics, (opto)spintronics, sensing and catalysis.

Acknowledgements

The authors thank the "ENSEMBLE3 - Centre of Excellence for nanophotonics, advanced materials and novel crystal growth-based technologies" project (GA No. MAB/2020/14) carried out within the International Research Agendas programme of the Foundation for Polish Science co-financed by the European Union under the European Regional Development Fund and the European Union's Horizon 2020 research and innovation programme Teaming for Excellence (GA. No. 857543) for support of this work. We thank the National Natural Science Foundation of China (Grant No. 21973059) for financial support and the Helmholtz-Zentrum Berlin für Materialien und Energie for the allocation of synchrotron radiation beamtimes. A.M. and D.S. acknowledge the BMBF (grant no. 05K19KER and 0519ODR, respectively). We acknowledge MAX IV Laboratory for time on Beamline FlexPES under Proposal 20210743. Research conducted at MAX IV, a Swedish national user facility, is supported by the Swedish Research council under contract 2018-07152, the Swedish Governmental Agency for Innovation Systems under contract 2018-04969, and Formas under contract 2019-02496. We highly appreciate the support by Dr. Alexei Preobrajenski during beamtime at MAX IV. The North-German Supercomputing Alliance (HLRN) is acknowledged for providing the computer time.

References

[1] Liu J, Wang Z, Su K, Xv D, Zhao D, Li J, Tong H, Qian D, Yang C and Lu Z 2019 *ACS Appl. Mater. Interfaces* **11** 25854–25862

[2] Wang D, Li Q, Han C, Xing Z and Yang X 2019 *Appl. Catal. B* **249** 91–97

[3] Wang S, Lu A and Zhong C J 2021 *Nano Convergence* **8** 4

[4] Sun L, Luo Q, Dai Z and Ma F 2021 *Coordin. Chem. Rev.* **444** 214049

[5] Lee J E, Jeon K J, Show P L, Lee I H, Jung S C, Choi Y J, Rhee G H, Lin K Y A and Park Y K 2022 *Fuel* **308** 122048

[6] Li X, Shen R, Ma S, Chen X and Xie J 2018 *Appl. Surf. Sci.* **430** 53–107

[7] Li D, Shi J and Li C 2018 *Small* **14** 1704179

[8] Wang J, Yue X, Yang Y, Sirisomboonchai S, Wang P, Ma X, Abudula A and Guan G 2019 *J. Alloy Compd.* **819** 153346

[9] Xia X, Wang L, Sui N, Colvin V L and Yu W W 2020 *Nanoscale* **12** 12249–12262

[10] Machado B F and Serp P 2011 *Catal. Sci. Technol.* **2** 54–75

[11] Li Q, He Y and Peng R 2015 *RSC Adv.* **5** 24507–24512

[12] Fujishima A and Honda K 1972 *Nature* **238** 37–38

[13] Ganguly P, Harb M, Cao Z, Cavallo L, Breen A, Dervin S, Dionysiou D D and Pillai S C 2019 *ACS Energy Lett.* **4** 1687–1709

[14] Ahmad H, Kamarudin S, Minggu L and Kassim M 2015 *Renew. Sustain. Energy Rev.* **43** 599–610

[15] Xue Y, Zhao G, Yang R, Chu F, Chen J, Wang L and Huang X 2021 *Nanoscale* **13** 3911–3936

[16] Ong W J, Tan L L, Ng Y H, Yong S T and Chai S P 2016 *Chem. Rev.* **116** 7159–7329

[17] Peng W, Li Y, Zhang F, Zhang G and Fan X 2017 *Ind. Eng. Chem. Res.* **56** 4611–4626

[18] Du C F, Liang Q, Dangol R, Zhao J, Ren H, Madhavi S and Yan Q 2018 *Nano-Micro. Lett.* **10** 67

[19] Zhang G, Zhang X, Meng Y, Pan G, Ni Z and Xia S 2020 *Chem. Eng. J.* **392** 123684

[20] Liu J, Li X B, Wang D, Lau W M, Peng P and Liu L M 2014 *J. Chem. Phys.* **140** 054707

[21] Zhang X, Zhao X, Wu D, Jing Y and Zhou Z 2016 *Adv. Sci.* **3** 1600062

[22] Du K z, Wang X z, Liu Y, Hu P, Utama M I B, Gan C K, Xiong Q and Kloc C 2016 *ACS Nano* **10** 1738–1743

[23] Yang J, Zhou Y, Dedkov Y and Voloshina E 2020 *Adv. Theory Simul.* **3** 2000228

[24] Yan M, Jin Y, Wu Z, Tsaturyan A, Makarova A, Smirnov D, Voloshina E and Dedkov Y 2021 *J. Phys. Chem. Lett.* **12** 2400–2405

[25] Wang S, Xiao B, Shen S, Song K, Lin Z, Wang Z, Chen Y and Zhong W 2020 *Nanoscale* **12** 14459–14464

[26] Das T, Alam K, Chakraborty S and Sen P 2021 *Int. J. Hydrogen. Energ.* **46** 37928–37938

[27] Kang S, Kim K, Kim B H, Kim J, Sim K I, Lee J U, Lee S, Park K, Yun S, Kim T, Nag A, Walters A, Garcia-Fernandez M, Li J, Chapon L, Zhou K J, Son Y W, Kim J H, Cheong H and Park J G 2020 *Nature* **583** 785–789

[28] Yang J, Zhou Y, Guo Q, Dedkov Y and Voloshina E 2020 *RSC Adv.* **10** 851–864

[29] Jin Y, Yan M, Kremer T, Voloshina E and Dedkov Y 2022 *Sci. Rep.* **12** 735

[30] Budniak A K, Zelewski S J, Birowska M, Woźniak T, Bendikov T, Kauffmann Y, Amouyal Y, Kudrawiec R and Lifshitz E 2022 *Adv. Opt. Mater.* **10** 2102489

[31] Autieri C, Cuono G, Noce C, Rybak M, Kotur K M, Agrapidis C E, Wohlfeld K and Birowska M 2022 *J. Phys. Chem. C* **126** 6791–6802

[32] Jin Y, Yan M, Dedkov Y and Voloshina E 2022 *J. Mater. Chem. C* **10** 3812–3818

[33] Foot P J S, Katz T, Patel S N, Nevett B A, Pieecy A R and Balchin A A 1987 *Phys. Status Solidi* **100** 11–29

[34] Silipigni L, Marco G D, Salvato G and Grasso V 2005 *Appl. Surf. Sci.* **252** 1998–2005

[35] Mi M, Zheng X, Wang S, Zhou Y, Yu L, Xiao H, Song H, Shen B, Li F, Bai L, Chen Y, Wang S, Liu X and Wang Y 2022 *Adv. Funct. Mater.* **32** 2112750

[36] Wang F, Shifa T A, He P, Cheng Z, Chu J, Liu Y, Wang Z, Wang F, Wen Y, Liang L and He J 2017 *Nano Energy* **40** 673–680

[37] Cheng Z, Shifa T A, Wang F, Gao Y, He P, Zhang K, Jiang C, Liu Q and He J 2018 *Adv. Mater.* **30** 1707433

[38] Molodtsov S L, Fedoseenko S I, Vyalikh D V, Iossifov I E, Follath R, Gorovikov S A, Brzhezinskaya M M, Dedkov Y S, Püttner R, Schmidt J S, Adamchuk V K, Gudat W and Kaindl G 2009 *Appl. Phys. A* **94** 501–505

[39] Follath R, Hävecker M, Reichardt G, Lips K, Bahrdt J, Schäfers F and Schmid P 2013 *J. Phys.:*

Conf. Ser. **425** 212003
[40] Hendel S, Schäfers F, Hävecker M, Reichardt G, Scheer M, Bahrdt J and Lips K 2016 *AIP Conf. Proc.* **1741** 030038
[41] Kresse G and Hafner J 1993 *Phys. Rev. B* **47** 558–561
[42] Kresse G and Hafner J 1994 *J. Phys. Condens. Matter* **6** 8245
[43] Kresse G and Furthmüller J 1996 *Comp. Mater. Sci.* **6** 15–50
[44] Perdew J P, Burke K and Ernzerhof M 1996 *Phys. Rev. Lett.* **77** 3865–3868
[45] Blöchl P E 1994 *Phys. Rev. B* **50** 17953–17979
[46] Blöchl P E, Jepsen O and Andersen O K 1994 *Phys. Rev. B* **49** 16223–16233
[47] Anisimov V I, Zaanen J and Andersen O K 1991 *Phys. Rev. B* **44** 943–954
[48] Dudarev S L, Botton G A, Savrasov S Y, Humphreys C J and Sutton A P 1998 *Phys. Rev. B* **57** 1505–1509
[49] Heyd J, Scuseria G E and Ernzerhof M 2003 *J. Chem. Phys.* **118** 8207–8215
[50] Grimme S 2006 *J. Comput. Chem.* **27** 1787–1799
[51] Xu S, Wu Z, Dedkov Y and Voloshina E 2021 *J. Phys. Condens. Matter* **33** 354001
[52] Wu Z, Xu S, Zhou Y, Guo Q, Dedkov Y and Voloshina E 2021 *Adv. Theory Simul.* **4** 2100182
[53] Dedkov Y, Yan M and Voloshina E 2020 *Chem. Phys. Lett.* **754** 137627
[54] Jin Y, Yan M, Jin Y, Li K, Dedkov Y and Voloshina E 2022 *J. Phys. Chem C*, accepted, doi: 10.1021/acs.jpcc.2c05950
[55] Gota S, Guiot E, Henriot M and Gautier-Soyer M 1999 *Phys. Rev. B* **60** 14387–14395
[56] Yamashita T and Hayes P 2008 *Appl. Surf. Sci.* **254** 2441–2449
[57] Mukherjee D, Austeria P M and Sampath S 2016 *ACS Energy Lett.* **1** 367–372
[58] Mukherjee D, P M A and Sampath S 2018 *ACS Appl. Energy Mater.* **1** 220–231
[59] Son C Y, Kwak I H, Lim Y R and Park J 2016 *Chem. Commun.* **52** 2819–2822
[60] Owens-Baird B, Sousa J P S, Ziouani Y, Petrovykh D Y, Zarkevich N A, Johnson D D, Kolen'ko Y V and Kovnir K 2020 *Chem. Sci.* **11** 5007–5016
[61] Dedkov Y S, Generalov A, Voloshina E N and Fonin M 2011 *Phys. Status Solidi RRL* **5** 226–228

Table 1. Reference values $E - E_{VBM}$ (in eV) for the core-levels emission lines extracted from the high-resolution XPS spectra obtained in the laboratory conditions on freshly cleaved $FePX_3$ single crystals.

XPS line	$FePS_3$	$FePSe_3$
Fe $2p_{3/2}$	−708.20	−707.97
P $2p_{3/2}$	−131.25	−131.12
S $2p_{3/2}$	−161.66	—
Se $3p_{3/2}$	—	−160.57

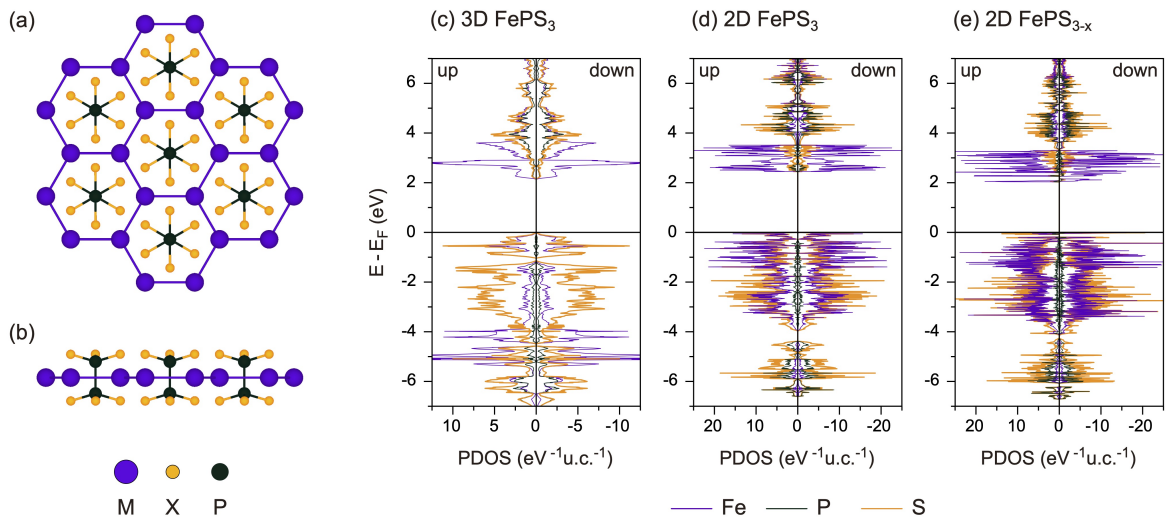

Figure 1. (a,b) Top and side views of a single layer of MPX_3. Spheres of different size/color represent ions of different type. (c-e) Site-projected density of states for: bulk $FePS_3$, pristine and defective $FePS_3$ monolayers.

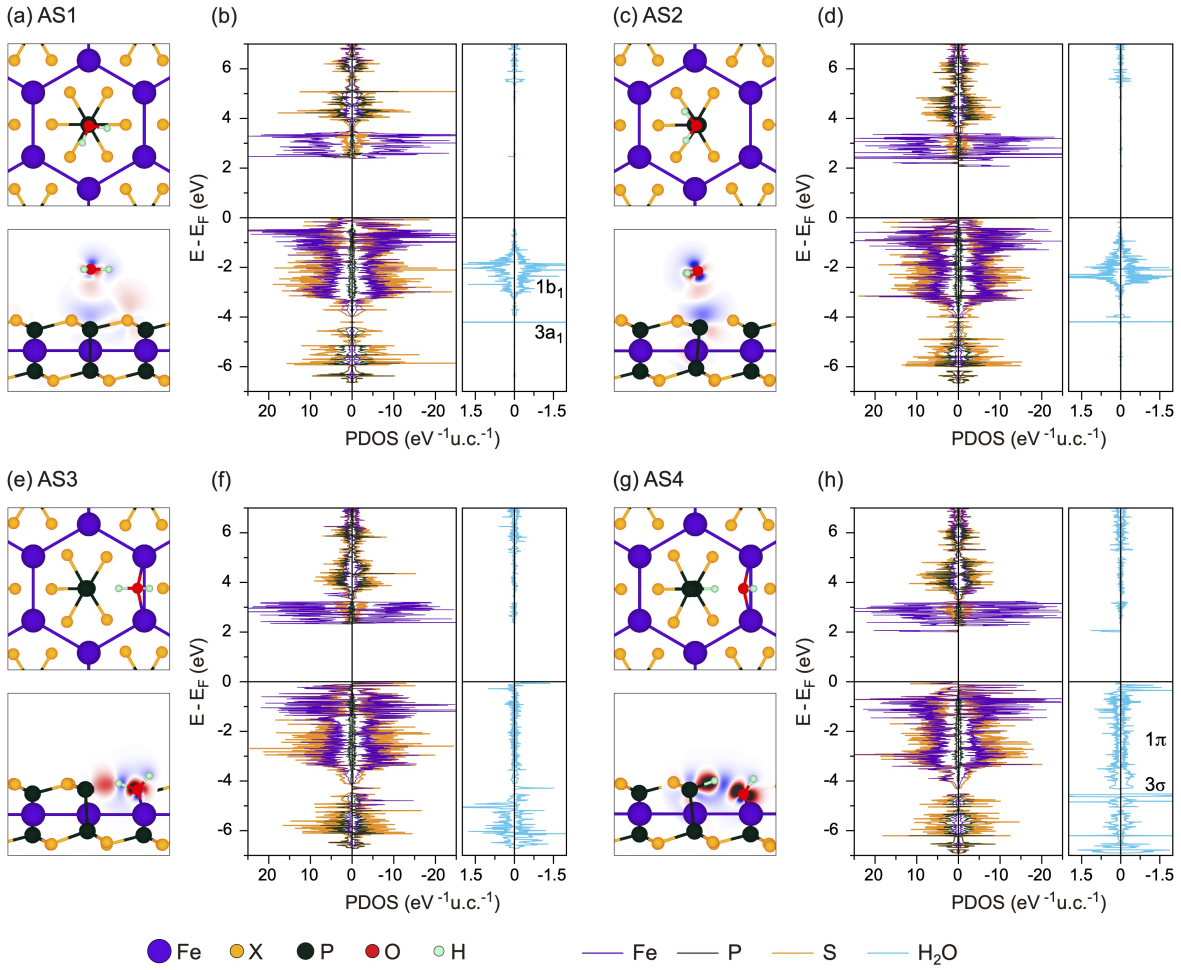

Figure 2. (a,c,e,g) Top and side views of the relaxed structures obtained after water adsorption on pristine and defective $FePX_3$ (see text for details). Spheres of different size/color represent ions of different type. Side views are superimposed with electron density redistribution maps. Electron density accumulation (depletion) is shown in red (blue). (b,d,f,h) Site-projected density of states obtained for the structures presented in (a,c,e,g) where X = S.

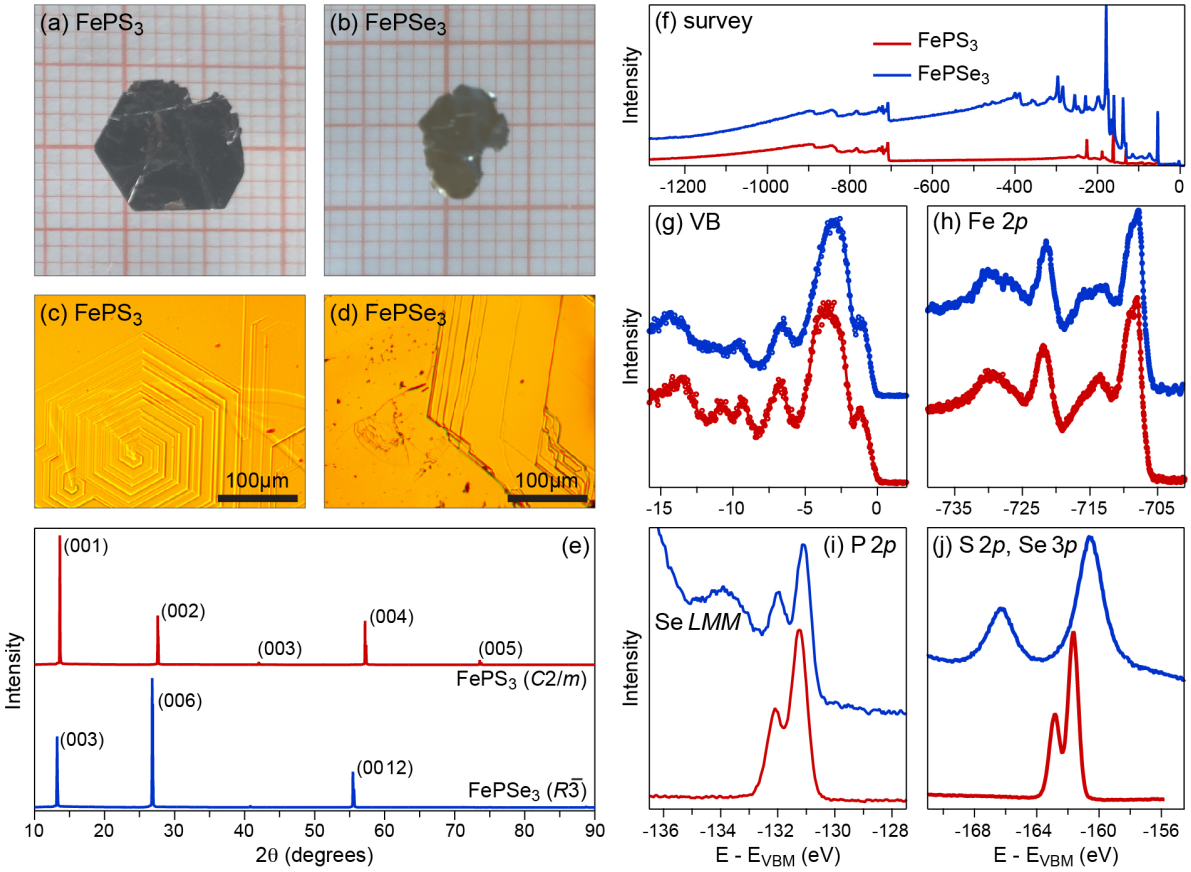

Figure 3. (a,b) Photos and (c,d) optical microscopy images of $FePX_3$ (X = S,Se), respectively. (e) XRD patterns for $FePX_3$ collected at room temperature using Cu K_α (1.54178 Å) radiation. XPS spectra obtained in the laboratory conditions on freshly cleaved $FePX_3$ single crystals: (f) survey spectra, (g) valence band, (h) Fe $2p$, (i) P $2p$, (j) S $2p$, Se $3p$. In (i) the large background originating from the Se LMM Auger emission line affects the P $2p$ spectra for $FePSe_3$. All spectra in (e-j) are vertically shifted for clarity.

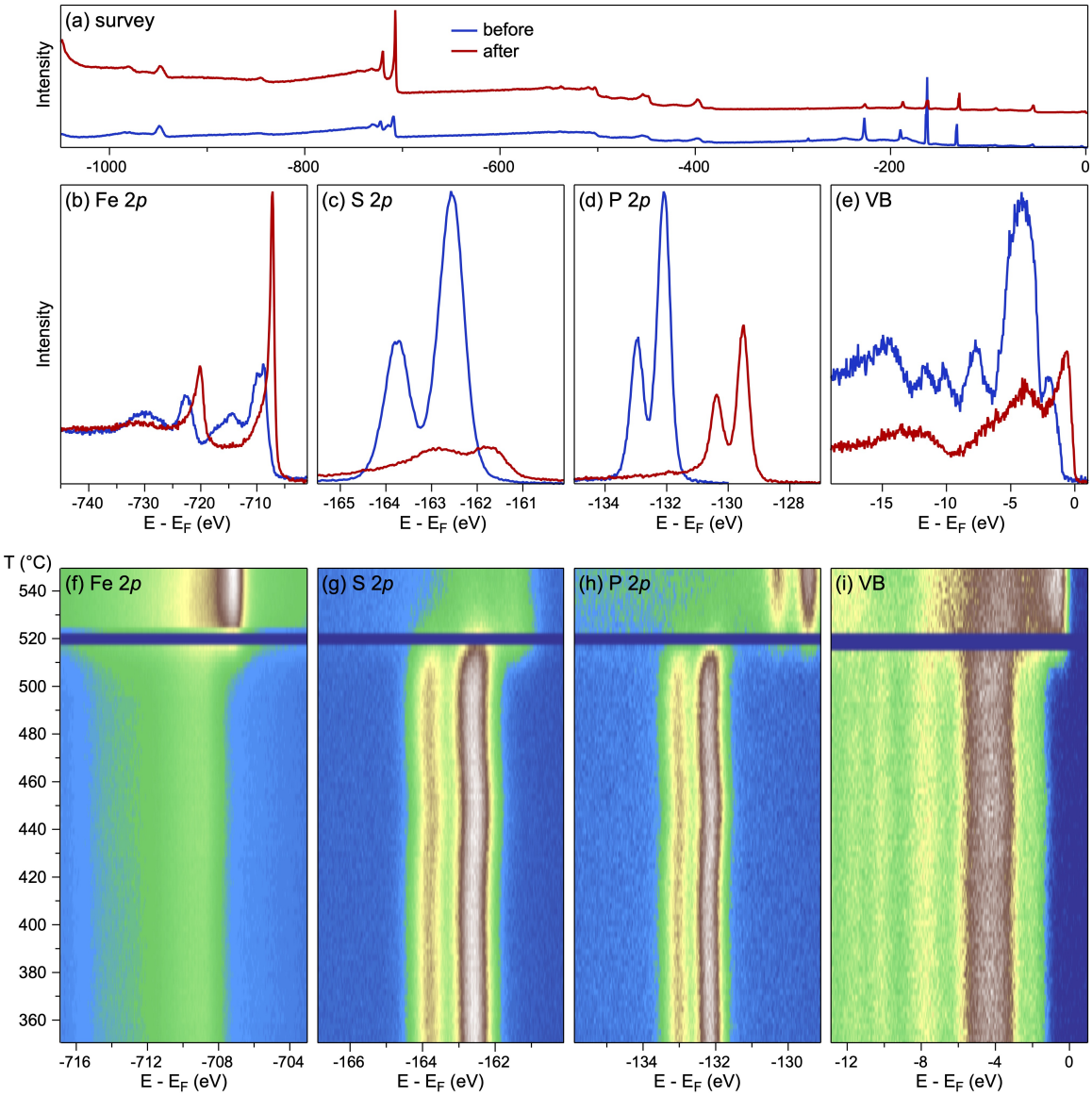

Figure 4. XPS spectra (measured at room temperature) collected for $FePS_3$ before and after temperature stability experiments: (a) survey, (b) Fe $2p$, (c) S $2p$, (d) P $2p$, (e) valence band. (f-i) Photoemission intensity maps based on the sequences of the respective XPS spectra collected in the "snapshot" mode of the analyzer as a function of the sample temperature. Spectra are shown in the temperature range of $350-550°$ C. The temperature gradient is 3 degrees/min. All spectra were collected at photon energy of $h\nu = 1000$ eV. Horizontal intensity drops in (f-i) are due to the closed last valve of the beamline when pressure in the chamber raised above the working limit.

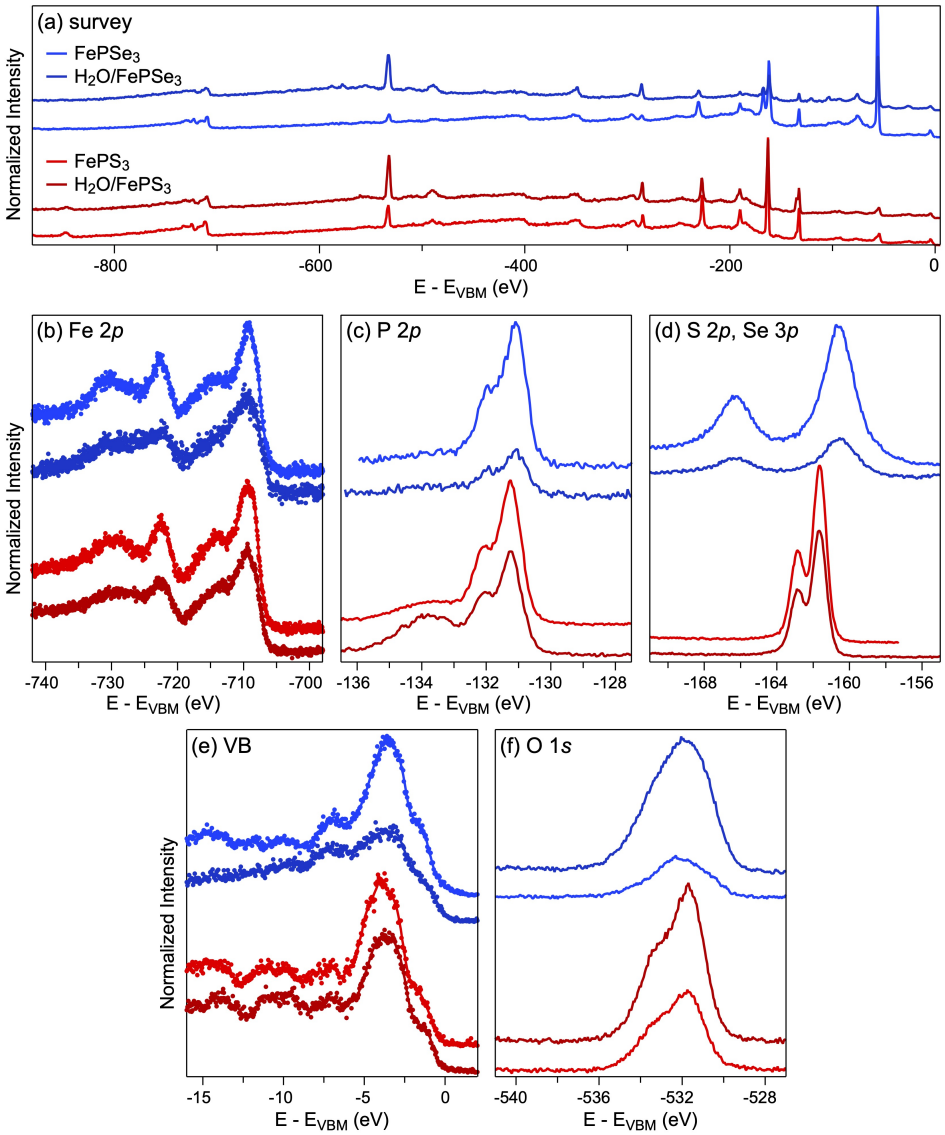

Figure 5. XPS spectra collected at the RGBL-dipole beamline using photon energy of $h\nu = 1000\,\mathrm{eV}$ before and after adsorption of 10 L of H_2O on $FePX_3$ at the sample temperature of 120 K: (a) survey spectra, (b) Fe $2p$, (c) P $2p$, (d) S $2p$, Se $3p$, (e) valence band, (f) O $1s$. All spectra are vertically shifted for clarity.

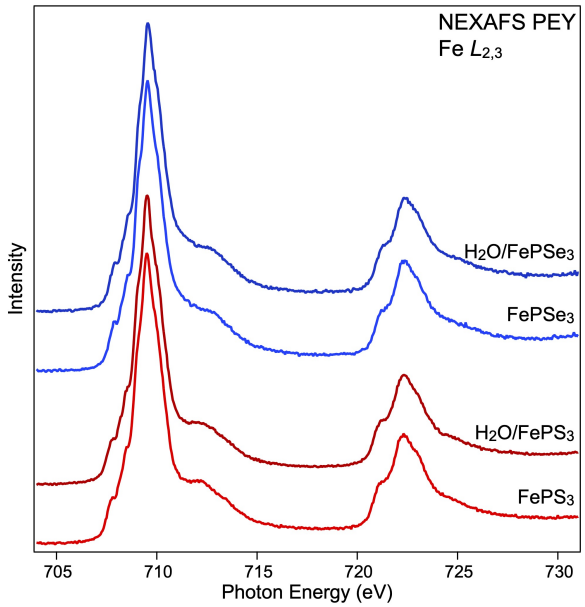

Figure 6. NEXAFS spectra of $FePX_3$ collected at the RGBL-dipole beamline in the PEY mode at the Fe $L_{2,3}$ absorption edge before and after adsorption of 10 L of H_2O at the sample temperature of 120 K. All spectra are vertically shifted for clarity.

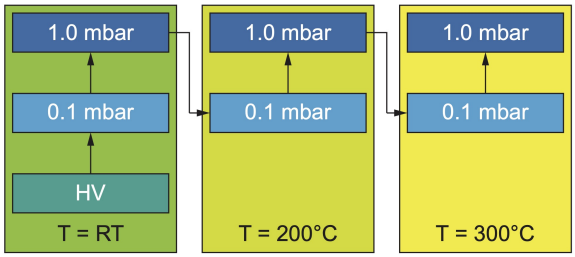

Figure 7. Temperature/water-pressure sequence during NAP-XPS/NEXAFS experiments on $FePX_3$.

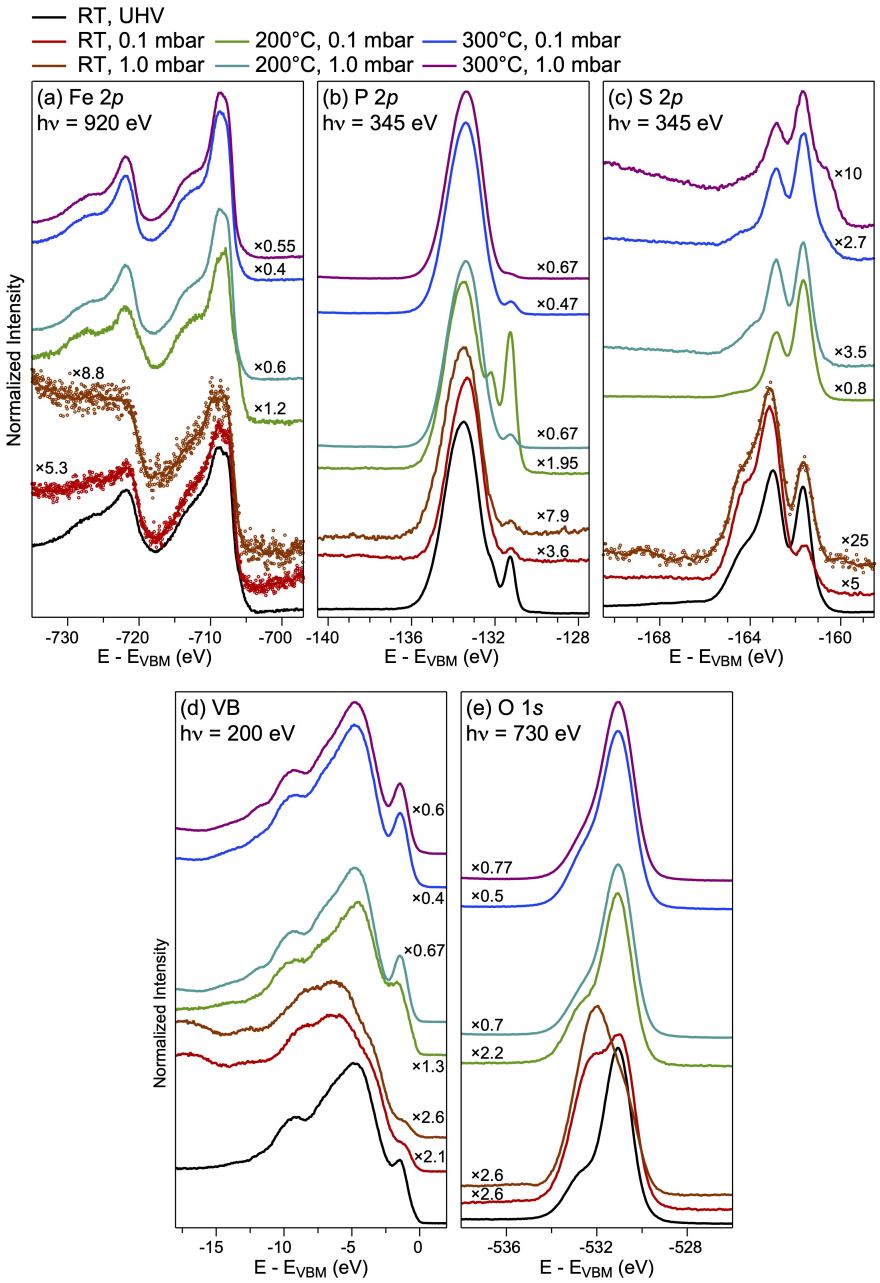

Figure 8. NAP-XPS spectra obtained for the $H_2O/FePS_3$ system: (a) Fe 2*p*, (b) P 2*p*, (c) S 2*p*, (d) valence band, (e) O 1*s*. The respective photon energies as well as applied temperatures and pressures of H_2O are marked in the plots. The intensity multiplication factors for every spectra are placed in the plots. All spectra are vertically shifted for clarity.

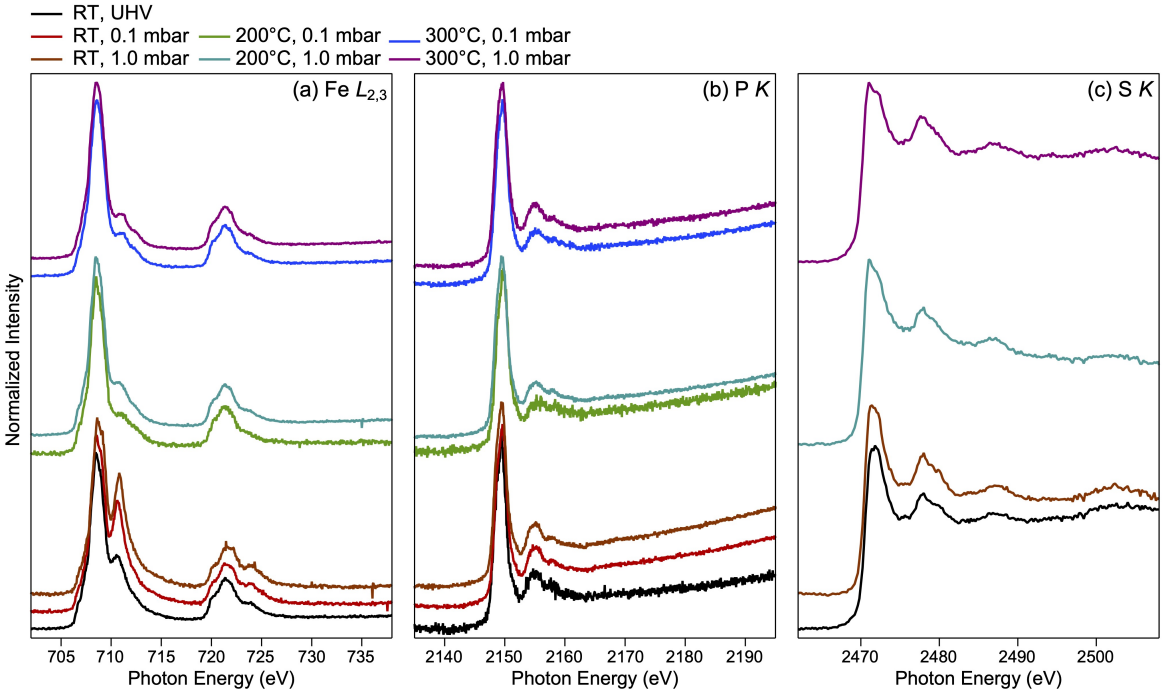

Figure 9. NAP-NEXAFS spectra obtained for the $H_2O/FePS_3$ system: (a) Fe $L_{2,3}$, (b) P K, (c) S K absorption edges. The applied temperatures as well as pressures of H_2O are marked in the plots. NEXAFS spectra were normalized to the maximum of intensity for every spectrum. All spectra are vertically shifted for clarity.